Spin-Pumping-Induced Inverse Spin Hall Effect in Nb/$Ni_{80}Fe_{20}$ Bilayers and its Strong Decay Across the Superconducting Transition Temperature

Kun-Rok Jeon,[1,2,*] Chiara Ciccarelli,[2] Hidekazu Kurebayashi,[3] Jöerg Wunderlich,[4,5] Lesley F. Cohen,[6] Sachio Komori,[1] Jason W. A. Robinson,[1] and Mark G. Blamire[1]

[1] *Department of Materials Science and Metallurgy, University of Cambridge, 27 Charles Babbage Road, Cambridge CB3 0FS, United Kingdom*
[2] *Cavendish Laboratory, University of Cambridge, Cambridge CB3 0HE, United Kingdom*
[3] *London Centre for Nanotechnology and Department of Electronic and Electrical Engineering, University of College London, London WC1H 01H, United Kingdom*
[4] *Hitachi Cambridge Laboratory, J. J. Thomson Avenue, Cambridge CB3 0HE, United Kingdom*
[5] *Institute of Physics, ASCR, Cukrovarnicka 10, 162 00 Praha 6, Czech Republic*
[6] *The Blackett Laboratory, Imperial College London, SW7 2AZ, United Kingdom*

(Received 26 March 2018; revised manuscript received 28 May 2018; published 27 July 2018)

We quantify the spin Hall angle θ_{SH} and spin-diffusion length l_{sd} of Nb from inverse spin Hall effect (ISHE) measurements in Nb/$Ni_{80}Fe_{20}$ bilayers under ferromagnetic resonance. By varying the Nb thickness t_{Nb} and comparing to a $Ni_{80}Fe_{20}$/Pt reference sample, room temperature values of θ_{SH} and l_{sd} for Nb are estimated to be approximately −0.001 and 30 nm, respectively. We also investigate the ISHE as a function of temperature T for different t_{Nb}. Above the superconducting transition temperature T_c of Nb, a clear t_{Nb}-dependent T evolution of the ISHE is observed whereas below T_c, the ISHE voltage drops rapidly and is below the sensitivity of our measurement setup at a lower T. This suggests the strong decay of the quasiparticle (QP) charge-imbalance relaxation length across T_c, as supported by an additional investigation of the ISHE in a different sample geometry along with model calculation. Our finding suggests careful consideration should be made when developing superconductor spin Hall devices that intend to utilize QP-mediated spin-to-charge interconversion.

DOI: 10.1103/PhysRevApplied.10.014029

I. INTRODUCTION

The flow of spin angular momentum without an accompanying net charge current, so-called pure spin current, is a key ingredient of spintronic devices mostly consisting of ferromagnet (FM) and nonmagnet (NM) heterostructures. This pure spin current enables us to transmit spin information through the NM with low-energy dissipation and to control the magnetization M of the FM via spin-transfer torque [1–5]. It has been well-established that ferromagnetic resonance (FMR) spin pumping [6,7], the dynamic transfer of spin angular momentum from a precessing FM into an adjacent NM, can provide an attractive and powerful method for generating the pure spin current.

The combination of FMR spin pumping with inverse spin Hall effect (ISHE) [8–10], spin-to-charge conversion, allows for the electrical detection of the generated spin currents in a FM or NM bilayer. A dynamically injected spin current J_s in the NM layer is converted into a transverse charge current J_c via the ISHE, producing a measurable electromotive force [Fig. 1(a)]. This approach has been widely employed to investigate the spin-orbit coupling and spin-transport parameters, such as spin Hall angle θ_{SH} and spin-diffusion length l_{sd}, in a variety of NM materials, including metals [9], semiconductors [11,12], oxide interfaces [13,14], and topological insulators [15,16].

Recent progress in superconducting spintronics [17,18] has highlighted the potential of superconductors (SCs) towards future low-energy computing technologies. Several studies exploring the quasiparticle (QP) spin transport in SCs have been achieved using dc (non)local transport measurements [18–25]. Interestingly, it has been shown that in all metallic nonlocal spin Hall devices with transparent contacts [25], the QP-mediated ISHE in the superconducting state of NbN increases significantly by about three orders of magnitude compared to that in the normal state. Another recent experiment has reported that for a ferrimagnetic insulator YIG/NbN junction with ohmic contacts [26], the ISHE voltage induced by the spin Seebeck effect is enhanced by a factor of approximately 2.5 in the vicinity of the superconducting transition. Although more work is certainly needed, these experiments seem to suggest the existence of emergent phenomena arising through QP spin-orbit coupling. This motivates us to investigate

*jeonkunrok@gmail.com

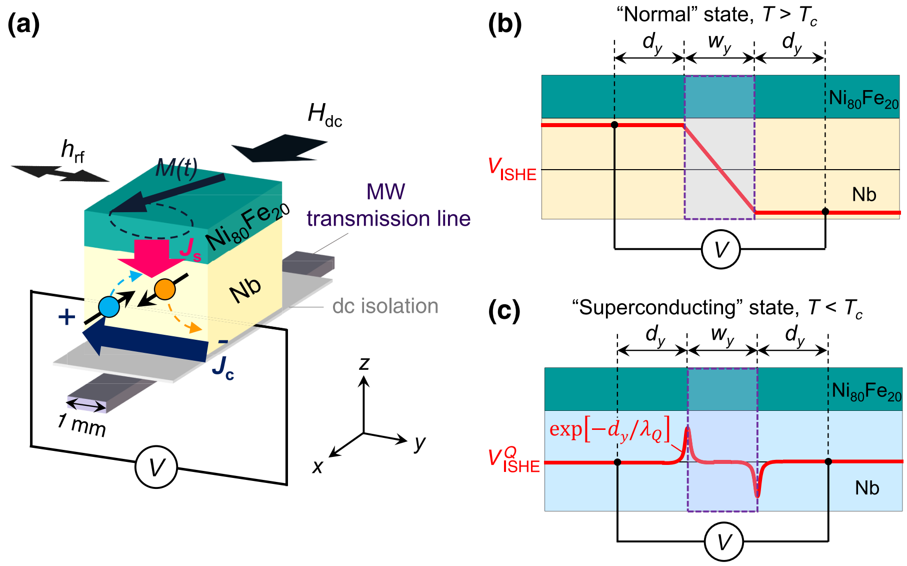

FIG. 1. (a) Sketch of the experimental setup used to dynamically inject a pure spin current J_s and electrically detect a (transverse) charge current J_c converted via inverse spin-Hall effect in a Nb/$Ni_{80}Fe_{20}$ bilayer. (b),(c) Spatial profile of the inverse spin-Hall voltage $V^{(Q)}_{\mathrm{ISHE}}$ induced by spin pumping in a Nb/$Ni_{80}Fe_{20}$ bilayer above and below the superconducting transition temperature T_c of Nb. In (c), $\exp[-d_y/\lambda_Q]$ describes the spatial decay of the charge-imbalance effect, where λ_Q is the quasiparticle charge-imbalance relaxation length and d_y is the distance between the inside edges of the precessing $Ni_{80}Fe_{20}$ and the voltage contact. The wine dashed line represents the active regime of ferromagnetic resonance in the $Ni_{80}Fe_{20}$. Note that the lateral dimension of the sample is much larger than the spin-diffusion length of Nb.

the QP-mediated ISHE in Nb, the standard material for superconducting electronics and spintronics.

Here, we experimentally quantify the θ_{SH} and l_{sd} values of Nb films from spin-pumping-induced ISHE measurements in Nb/$Ni_{80}Fe_{20}$ bilayers by varying the Nb thickness t_{Nb} and comparison with a $Ni_{80}Fe_{20}$/Pt reference sample. Spin-precession effect under an oblique magnetic field also enables a first-order estimate of the spin lifetime in the Nb. Furthermore, we study the ISHE as a function of temperature T for different t_{Nb}. Above the superconducting transition temperature T_c of Nb, a clear t_{Nb}-dependent T evolution of the ISHE is observed. Yet below T_c, the ISHE voltage drops rapidly and becomes unmeasurable at a lower T, which can be explained by the short QP charge-imbalance relaxation length in the superconducting Nb. Our experiments along with model calculation suggest the necessity of a careful design of the sample or device geometry in spin-pumping-induced ISHE measurements with SCs below T_c.

II. EXPERIMENTAL DETAILS

We prepare Nb/$Ni_{80}Fe_{20}$ structures, $Ni_{80}Fe_{20}$/Nb inverted structures, and Pt/$Ni_{80}Fe_{20}$ reference samples on either thermally oxidized Si or quartz substrates with lateral dimension of 3–5 mm $\times$ 5 mm by dc magnetron sputtering in an ultra-high vacuum chamber. Note that the $Ni_{80}Fe_{20}$/Nb inverted structures are used for the study of the sample geometry dependence by simplifying the patterning process. While t_{Nb} ranges from 7.5 to 60 nm, the $Ni_{80}Fe_{20}$ (Pt) thickness is fixed at 6 nm (5 nm). Details of the sample preparation can be found elsewhere [27].

The T_c of the Nb layers is determined by dc electrical transport measurements (see Ref. [28]). Hereafter, T_c denotes the value determined under microwave excitation unless otherwise specified. Single-stripe-patterned samples are prepared by conventional microfabrication techniques (e.g., photolithography, Ar-ion beam etching).

The measurement setup used for this study [Fig. 1(a)] is based on broad-band FMR techniques [27]. The sample is attached face down on the coplanar waveguide (CPW) by using an electrically insulating high-vacuum grease. A MW signal is passed through the CPW and excited FMR of the $Ni_{80}Fe_{20}$ layer; a transverse dc voltage as a function of external static magnetic field is measured between two Ag-paste contacts at opposite ends of the sample. *Simultaneously*, we measure the absorbed MW power where the FMR is excited. We employ a vector field cryostat from *Cryogenic Ltd* that allows for a 1.2 T magnetic field in any direction over a wide T range of 2–300 K.

III. RESULTS AND DISCUSSION

A. Nb thickness dependence of inverse spin Hall effect in Nb/$Ni_{80}Fe_{20}$ bilayers

We start by describing the spin-pumping-induced ISHE in Nb/$Ni_{80}Fe_{20}$ samples at 300 K. Figure 2 shows the FMR absorption (top panel) and transverse dc voltage measurements (bottom panel) vs external magnetic field $\mu_0 H$ along the x axis for three different t_{Nb} (7.5, 30, and 60 nm). In these measurements, the MW frequency is fixed at 5 GHz and the MW power at the CPW at approximately 100 mW. In all the samples, the FMR of the $Ni_{80}Fe_{20}$ is excited around the resonance magnetic field $\mu_0 H_{\mathrm{res}}$ and a clear

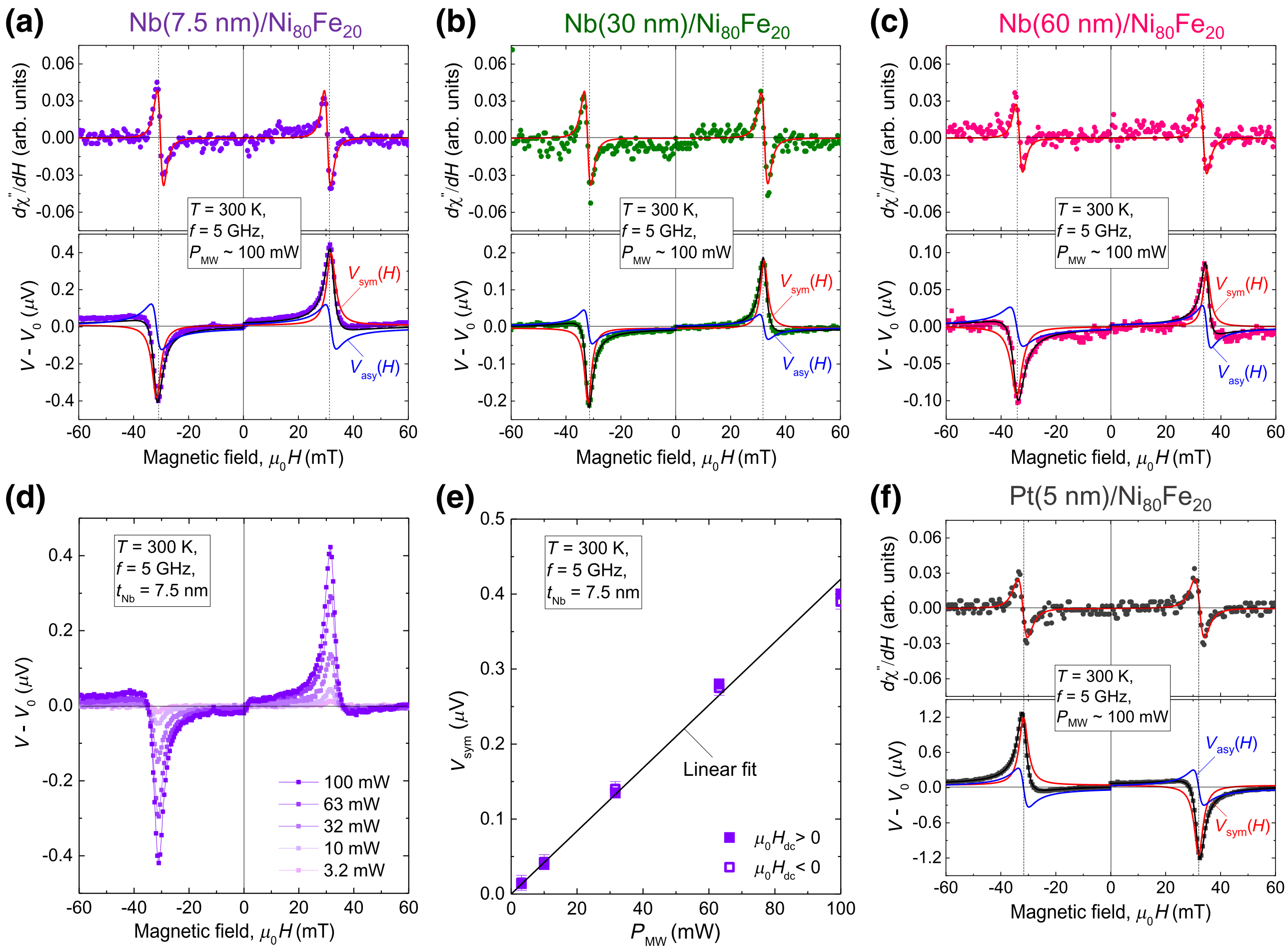

FIG. 2. (a)–(c) Ferromagnetic resonance absorption (top panel) and dc voltage measurements (bottom panel) vs external magnetic field $\mu_0 H$ (along the x axis) for the Nb/$Ni_{80}Fe_{20}$ sample with three different Nb thicknesses t_{Nb} (7.5, 30, and 60 nm) at 300 K. In these measurements, the MW frequency is fixed at 5 GHz and the MW power at the CPW at approximately 100 mW. The solid lines are fits to Lorentzian functions [Eq. (1)]. (d),(e) Typical example of the P_{MW} dependence of symmetric Lorentzian V_{sym}, extracted from fitting Eq. (1) to the data of $t_{Nb} = 7.5$ nm [Fig. 2(d)]. The black solid line is a linear fit. (f) The data shown are similar to that in (a)–(c) but now for the the Pt(5 nm)/$Ni_{80}Fe_{20}$ reference sample.

Lorentzian peak emerges in the dc voltage. Importantly, the polarity of the Lorentzian peak is inverted by reversing the magnetic field, which is consistent with the symmetry of ISHE [8–10].

The measured (dc) voltage can be decomposed into symmetric and antisymmetric Lorentzian functions with respect to $\mu_0 H_{res}$, with weights of V_{sym} and V_{asy} respectively:

$$\begin{aligned} V(H) &= V_{sym}(H) + V_{asy}(H) + V_0, \\ V_{sym}(H) &= V_{sym}\left[\frac{(\Delta H)^2}{(\Delta H)^2 + (H - H_{res})^2}\right], \\ V_{asy}(H) &= V_{asy}\left[\frac{(\Delta H)\cdot(H - H_{res})}{(\Delta H)^2 + (H - H_{res})^2}\right], \end{aligned} \tag{1}$$

where V_0 is a background voltage. All the data are well fitted by Eq. (1). We note that, in principle, V_{sym} is attributed not only to the ISHE but also to the spin-rectification effect (SRE) [29–31]. However, in our setup the ISHE contribution turns out to be predominant, as discussed in more detail below.

A typical MW power (P_{MW}) dependence of V_{sym}, extracted from the data $t_{Nb} = 7.5$ nm [Fig. 2(d)], is shown in Fig. 2(e). The extracted V_{sym} scales almost linearly with P_{MW}, as expected for the FMR spin pumping in the linear-response regime ($J_s \propto P_{MW}$) [8–10]. To check the sign of θ_{SH} in Nb, we repeat the same measurement on a Pt/$Ni_{80}Fe_{20}$ reference sample [Fig. 2(f)], where the Pt is well known to have a positive θ_{SH} [8,9,32]. Opposite signs of V_{sym} are observed in the Nb and Pt spin-sink samples [Figs. 2(a) and 2(f)], confirming the negative θ_{SH} of Nb [24,33]. Moreover, the sign change in V_{sym} indicates that

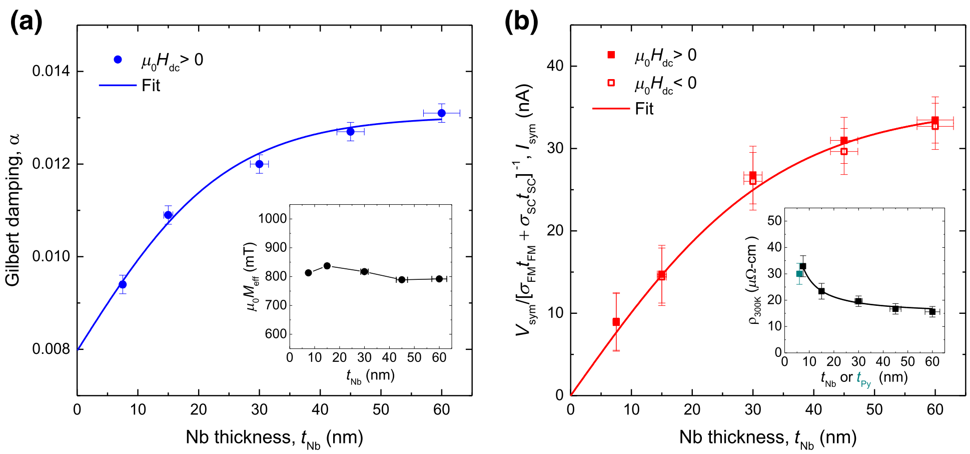

FIG. 3. (a) Effective Gilbert damping α as a function of Nb thickness t_{Nb}. The inset summarizes the effective saturation magnetization $\mu_0 M_{\mathrm{eff}}$ for each t_{Nb}. These are deduced from the MW frequency f dependence of FMR spectra (see Ref. [28]). Fitting Eq. (2) to the data (blue solid line) yields $g_r^{\uparrow\downarrow} = 16 \pm 3\ \mathrm{nm}^{-2}$ and $l_{\mathrm{sd}}^{\mathrm{SC}} = 35 \pm 2$ nm at 300 K. (b) Symmetric Lorentzian function of dc voltage V_{sym} as a function of t_{Nb}. The red solid line represents the room-temperature values obtained from Eq. (4) for $\theta_{\mathrm{SH}} \approx -0.001$ and $l_{\mathrm{sd}}^{\mathrm{SC}} \approx 30$ nm in Nb films.

the ISHE, rather than the SRE [8–10], gives a dominant contribution to V_{sym}.

To quantify the spin Hall angle θ_{SH} and the spin-diffusion length l_{sd} in the Nb films, we plot the effective Gilbert damping α [Fig. 3(a)] and V_{sym} [Fig. 3(b)] as a function of t_{Nb}. The values of α and the effective saturation magnetization $\mu_0 M_{\mathrm{eff}}$ [inset of Fig. 3(a)] are deduced from the MW frequency f dependence of FMR spectra (e.g., the FMR linewidth $\mu_0 \Delta H$ and the resonance field $\mu_0 H_{\mathrm{res}}$, see Ref. [28]). The t_{Nb}-dependent α enhancement, resulting from FMR spin pumping into the Nb layer [6,7], can be expressed by

$$\alpha(t_{\mathrm{SC}}) = \alpha_0 + \alpha_{\mathrm{sp}}(t_{\mathrm{SC}}),$$
$$\alpha_{\mathrm{sp}}(t_{\mathrm{SC}}) = \left(\frac{g_L \mu_B g_r^{\uparrow\downarrow}}{4\pi M_s t_{\mathrm{FM}}}\right)\left[1 + \frac{g_r^{\uparrow\downarrow}\mathcal{R}_{\mathrm{SC}}}{\tanh(t_{\mathrm{SC}}/l_{\mathrm{sd}}^{\mathrm{SC}})}\right]^{-1}, \tag{2}$$

where α_0 and α_{sp} are, respectively, the FMR damping irrelevant and relevant to the spin pumping, g_L is the Landé g factor taken to be 2.1 [34], and μ_B is the Bohr magneton. $g_r^{\uparrow\downarrow}$ is the effective real-part spin-mixing conductance across a Nb/$Ni_{80}Fe_{20}$ interface. $\mathcal{R}_{\mathrm{SC}} \equiv \rho_{\mathrm{SC}} l_{\mathrm{sd}}^{\mathrm{SC}} e^2/2\pi\hbar$ is the spin resistance, ρ_{SC} is the resistivity of the Nb [inset of Fig. 3(b)], and e is the electron charge. t_{FM} and t_{SC} are the $Ni_{80}Fe_{20}$ thickness (6 nm) and the Nb thickness (7.5–60 nm), respectively. Fitting Eq. (2) to $\alpha(t_{\mathrm{Nb}})$ [blue line in Fig 3(a)] yields $g_r^{\uparrow\downarrow} = 16 \pm 3\ \mathrm{nm}^{-2}$ and $l_{\mathrm{sd}}^{\mathrm{SC}} = 35 \pm 2$ nm at 300 K. The estimated $l_{\mathrm{sd}}^{\mathrm{SC}}$ is in the same range as reported previously for $Ni_{80}Fe_{20}$/Nb/$Ni_{80}Fe_{20}$ spin valves [20].

By combining the calculated spin-current density j_s at the Nb/$Ni_{80}Fe_{20}$ interface with the measured V_{sym} (or charge current I_c) [Fig. 3(b)], one can estimate the spin-to-charge conversion efficiency parameterized by θ_{SH}:

$$j_s \approx \left(\frac{G_r^{\uparrow\downarrow}\hbar}{8\pi}\right)\left(\frac{\mu_0 h_{\mathrm{rf}}\gamma}{\alpha}\right)^2 \times \left[\frac{\mu_0 M_{\mathrm{eff}}\gamma + \sqrt{(\mu_0 M_{\mathrm{eff}}\gamma)^2 + 16(\pi f)^2}}{(\mu_0 M_{\mathrm{eff}}\gamma)^2 + 16(\pi f)^2}\right]\left(\frac{2e}{\hbar}\right), \tag{3}$$

$$V_{\mathrm{ISHE}} = \left(\frac{R_{\mathrm{FM}}R_{\mathrm{SC}}}{R_{\mathrm{FM}} + R_{\mathrm{SC}}}\right) I_c = \left(\frac{w_y}{\sigma_{\mathrm{FM}}t_{\mathrm{FM}} + \sigma_{\mathrm{SC}}t_{\mathrm{SC}}}\right) \times \theta_{\mathrm{SH}} l_{\mathrm{sd}}^{\mathrm{SC}} \tanh\left(\frac{t_{\mathrm{SC}}}{2 l_{\mathrm{sd}}^{\mathrm{SC}}}\right) j_s, \tag{4}$$

where

$$G_r^{\uparrow\downarrow} \equiv g_r^{\uparrow\downarrow}\left[1 + g_r^{\uparrow\downarrow}\mathcal{R}_{\mathrm{SC}}/\tanh\left(\frac{t_{\mathrm{SC}}}{l_{\mathrm{sd}}^{\mathrm{SC}}}\right)\right]^{-1}.$$

$\gamma = g_L \mu_B/\hbar$ is the gyromagnetic ratio of $1.84 \times 10^{11}\ \mathrm{T}^{-1}\,\mathrm{s}^{-1}$ and $\hbar$ is Plank's constant divided by 2π. $\mu_0 h_{\mathrm{rf}}$ is the amplitude of MW magnetic field (0.15 mT for 100 mW) [35]. $R_{\mathrm{FM}}(R_{\mathrm{SC}})$ and $\sigma_{\mathrm{FM}}(\sigma_{\mathrm{SC}})$ are the square resistance and the conductivity of the $Ni_{80}Fe_{20}$ (Nb) layer [inset of Fig. 3(b)], respectively. w_y is the width of MW transmission line (1 mm, see Fig. 1) for the unpatterned samples. From the data in Fig. 3(b) using $g_r^{\uparrow\downarrow} = 16 \pm 3\ \mathrm{nm}^{-2}$ and Eq. (4), we obtain the room temperature (RT) values of $\theta_{\mathrm{SH}} \approx -0.001$ and $l_{\mathrm{sd}}^{\mathrm{SC}} \approx 30$ nm for the Nb film. This θ_{SH} value, corresponding to the spin Hall conductivity $\sigma_{\mathrm{SHE}} \approx -0.06 \times 10^3\,\Omega^{-1}\,\mathrm{cm}^{-1}$, is in good agreement with that expected from theoretical calculations [36]. We

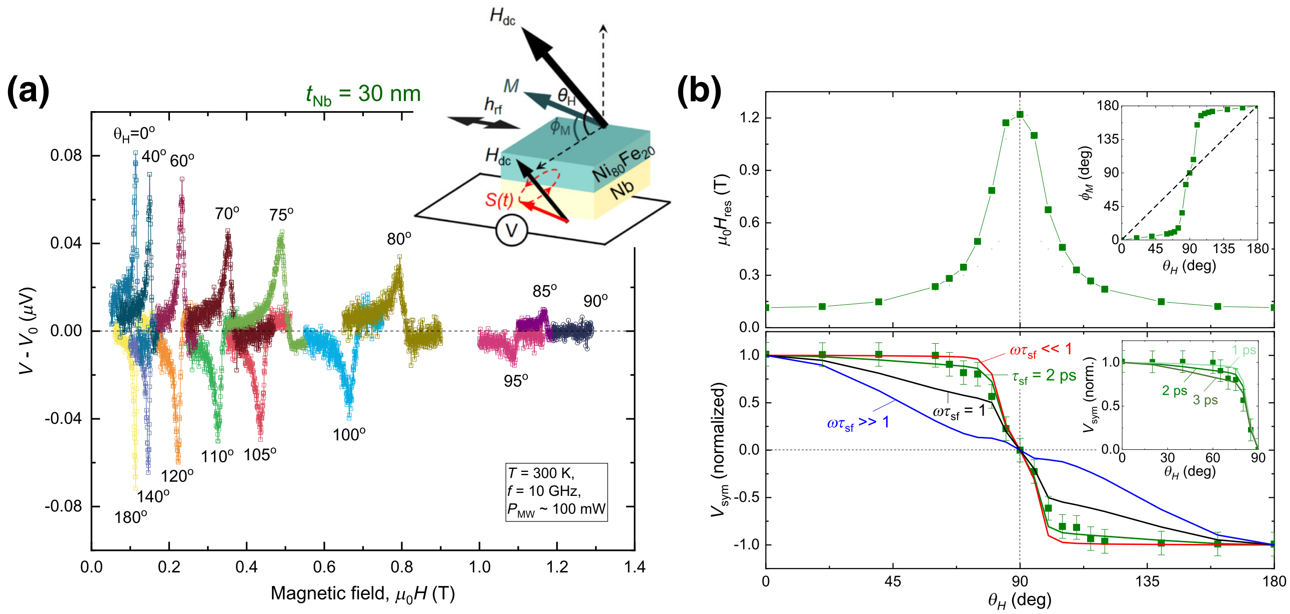

FIG. 4. (a) Out-of-plane magnetic-field-angle dependence of dc voltage $V - V_0$ obtained from the Nb(30 nm)/$Ni_{80}Fe_{20}$ sample, taken at a fixed MW frequency f of 10 GHz and MW power P_{MW} of approximately 100 mW. The inset illustrates schematically the measurement scheme. θ_H (ϕ_M) is the angle of external magnetic field (magnetization precession axis of FM) to the x axis. (b) Top panel, θ_H dependence of the resonance field. The upper inset displays the calculated ϕ_M as a function of θ_H using Eq. (5). (b) Bottom panel, θ_H dependence of the symmetric Lorentzian V_{sym}, extracted from fitting Eq. (1) to the data of (a). The measured $V_{sym}(\theta_H)$ is fairly reproduced by Eq. (6) with the spin lifetime τ_{sf} of the order of a few ps (lower inset). For comparison, the calculated $V_{ISHE}(\theta_H)$ using Eq. (6) with $\tau_{sf} \ll 1/\omega_L$ (red solid line), $\tau_{sf} = 1/\omega_L$ (black solid line), and $\tau_{sf} \gg 1/\omega_L$ (blue solid line) are also shown.

also note that in a previous experiment of the nonlocal spin valve with a rather resistive Nb ($\rho_{Nb} = 90\ \mu\Omega$ cm at 10 K), a larger θ_{SH} of -0.009 and a smaller l_{sd}^{SC} of 6 nm are obtained [33], giving $\sigma_{SHE} = -0.10 \times 10^3 \Omega^{-1}$ cm^{-1}. This value is similar to what we obtain.

B. Out-of-plane angular dependence and oblique Hanle spin precession

We measure the out-of-plane angular dependence of dc voltages [Fig. 4(a)] to extrapolate the spin lifetime τ_{sf} in Nb. The results discussed here corroborate that the observed V_{sym} signals are ascribed to the spin-pumping-induced ISHE in the Nb layer. When $\mu_0 H$ is applied at an angle θ_H to the x axis [inset of Fig. 4(a)], the angle ϕ_M of the M precession axis does not necessarily coincide with θ_H because of the demagnetization energy (or shape anisotropy energy). The corresponding misalignment angle $(\theta_H - \phi_M)$ on FMR is given by [37]

$$(\theta_H - \phi_M) \approx \arctan \left[\mathrm{sgn}(\theta_H)\sqrt{\left(\frac{\cos(2\theta_H)\ +\ (\mu_0 H_{res}/\mu_0 M_{eff})}{\sin(2\theta_H)}\right)^2 + 1} - \frac{\cos(2\theta_H)\ +\ (\mu_0 H_{res}/\mu_0 M_{eff})}{\sin(2\theta_H)} \right]. \quad (5)$$

The θ_H dependence of ϕ_M, calculated from Eq. (5) with the measured value of $\mu_0 H_{res}$ [Fig. 4(b), top panel], is shown in the inset of Fig. 4(b). This misalignment $(\theta_H - \phi_M)$ can give rise to the Hanle effect [38], in which the static $\mu_0 H$ transverse to the pumped spins $S(t)$ suppresses the spin accumulation in the spin sink via spin precession and dephasing [inset of Fig. 4(a)], if τ_{sf} is comparable to or longer than the Larmor precession time $1/\omega_L$. This results in the characteristic angular dependence of the voltage signal [39,40]:

$$V_{ISHE}(\theta_H) \propto \left\{ \cos(\theta_H)\cos(\theta_H - \phi_M) + \sin(\theta_H) \times \sin(\theta_H - \phi_M) \left[\frac{1}{1 + (\omega_L \tau_{sf})^2} \right] \right\}, \quad (6)$$

with $\omega_L = g_L \mu_B(\mu_0 H)/\hbar$ is the Larmor frequency. It is worth noting that in the case of a short τ_{sf} [red symbol in Fig. 4(b)], $V_{ISHE}(\theta_H)$ is simply proportional to $\cos(\phi_M)$. On the other hand, if τ_{sf} increases [$\geq 1/\omega_L$, black and blue symbols in Fig. 4(b)], the Hanle spin precession effectively reduces $V_{ISHE}(\theta_H)$ in particular around $\theta_H = 80°$, where the absolute of $(\theta_H - \phi_M)$ is maximun [upper inset of Fig. 4(b)]. The measured $V_{sym}(\theta_H)$ in the $Nb/Ni_{80}Fe_{20}$ bilayer is fairly reproduced by Eq. (6) with τ_{sf} of the order of a few ps [lower inset of Fig. 4(b)]. This is also consistent with the estimated value of 2–3 ps using $\tau_{sf}^{SC} = (l_{sd}^{SC})^2/D_{SC}$, where D_{SC} is the diffusion

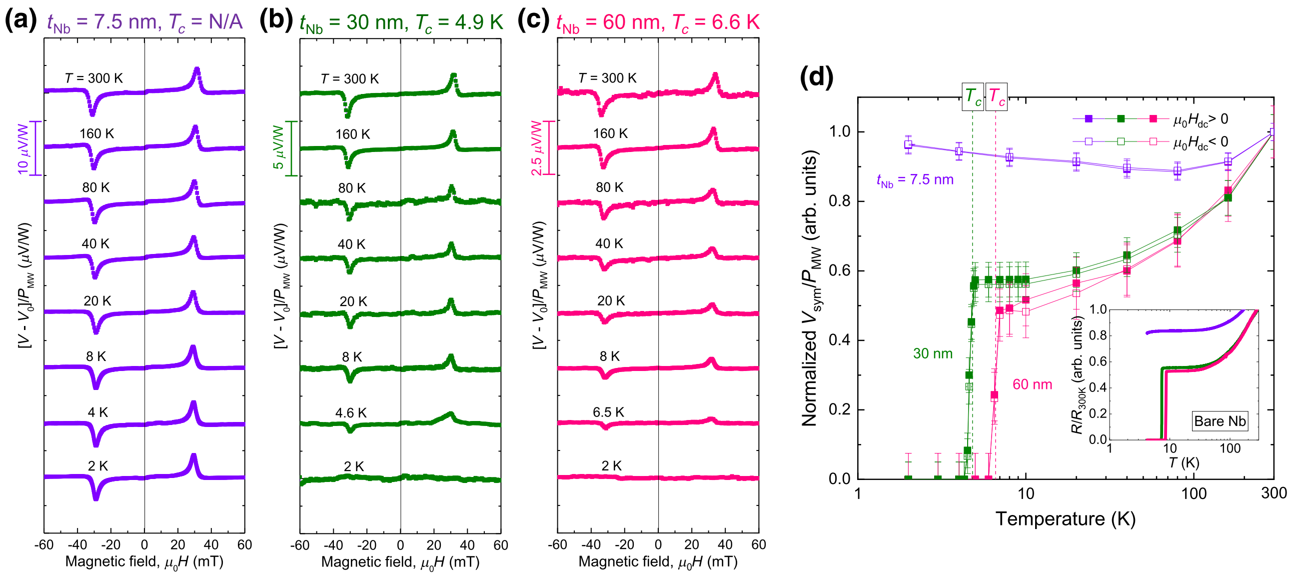

FIG. 5. (a)–(c) Temperature T evolution of dc voltage $V - V_0$ for the $Nb/Ni_{80}Fe_{20}$ samples with three different Nb thicknesses t_{Nb} of 7.5, 30, and 60 nm, taken at a fixed MW frequency f of 5 GHz. Note that for more quantification, the $V - V_0$ value is normalized by the MW power P_{MW}. (d) T dependence of the normalized symmetric Lorentzian function V_{sym}/P_{MW}, extracted from fitting Eq. (1) to the data of (a), for $t_{Nb} = 7.5$, 30, and 60 nm. The inset shows the normalized resistance R/R_{300K} vs the T plot for bare Nb films.

coefficient of Nb (10–15 cm^2/s at RT) and $l_{sd}^{SC} \approx 30$ nm is obtained from $V_{sym}(t_{Nb})$ [Fig. 3(b)]. The ISHE in a $Ni_{80}Fe_{20}$ layer could, in principle, contribute to $V_{ISHE}(\theta_H)$ [41]. However, $\tau_{sf} = 0.025$ ps in the $Ni_{80}Fe_{20}$ calculated using $D_{FM} = 10$ cm^2/s and $l_{sd}^{FM} = 5$ nm [42] is too short ($\ll 1/\omega_L \approx 8$ ps for $\mu_0 H_{res} = 0.7$–0.8 T around $\theta_H = 80°$) to cause the noticeable suppression of V_{ISHE}. This result further confirms that the measured V_{sym} signals in our system originate from the spin-pumping-induced ISHE in the Nb layer.

C. Temperature evolution of spin-pumping-induced inverse spin Hall effect

Next, we investigate the T dependence of V_{sym} for the $Nb/Ni_{80}Fe_{20}$ samples with three different t_{Nb} of 7.5, 30, and 60 nm [Fig. 5(a)]. As summarized in Fig. 5(b), for $t_{Nb} = 7.5$ nm (nonsuperconducting down to 2 K), V_{sym} is visible in the entire T range, varying slightly as T decreases. In contrast, for the thicker superconducting samples ($t_{Nb} = 30$ and 60 nm), V_{sym} is reduced gradually with decreasing T from 300 to 10 K. When $T < 8$ K (entering the superconducting state), the voltage signal drops abruptly and becomes below the sensitivity of our measurement setup at a lower T. The t_{Nb}-dependent T evolution of V_{sym} in the normal state is qualitatively understood in terms of the t_{Nb}-dependent T evolution of ρ_{Nb} [inset of Fig. 4(d)] and $G_r^{\uparrow\downarrow}$ [see Eqs. (3) and (4)]. Note that the trade-off of the ρ_{Nb} reduction and the $G_r^{\uparrow\downarrow}$ enhancement with decreasing T determines the overall T dependence of V_{ISHE}. In our system, we observe no clear signature of the coherence effect of superconductivity (see Ref. [28] for detailed data), namely, anomalous enhancement of spin-current flow near T_c that results from the well-developed coherence peaks of the SC DOS being accessible to the spin-transporting QPs [26,43,44]. This supports the previous studies [43–45] that for a *metallic/conducting* FM in direct contact with SC, Δ is significantly suppressed at the FM-SC interface due to the (inverse) proximity effect of the FM, leading to the vanishing of the superconducting coherence peak effect [43–45]. How local T increase due to MW power absorption influences the voltage signal immediately below T_c is also discussed in Ref. [28].

D. Model calculation of quasiparticle-mediated spin Hall voltages in Nb films

To understand why the ISHE voltages (in our setup) have vanished deep into the superconducting state, we consider the decay of the charge imbalance effect caused by nonequilibrium electronlike or holelike QP states [23,25,46,47], namely, the charge-imbalance relaxation length λ_Q. In the diffusive case, l_{sd} is longer than the mean free path l_{mfp} [46–48],

$$\lambda_Q = \sqrt{D_Q \tau_Q}, \quad \tau_Q \approx \frac{4 k_B T}{\pi \Delta(T)} \tau_\varepsilon, \tag{7}$$

where $D_Q = [2 f_0(\Delta)/\chi_Q^0(T)] D$ is the charge-diffusion coefficient of the QPs [49,50], $f_0(\Delta) = [\exp(\Delta/k_B T) + 1]^{-1}$ is the Fermi-Dirac (FD) distribution function at Δ, and $\chi_Q^0(T) = 2\int_\Delta^\infty (\sqrt{E^2 - \Delta^2}/E)[-\partial f_0(E)/\partial E] dE$ is the

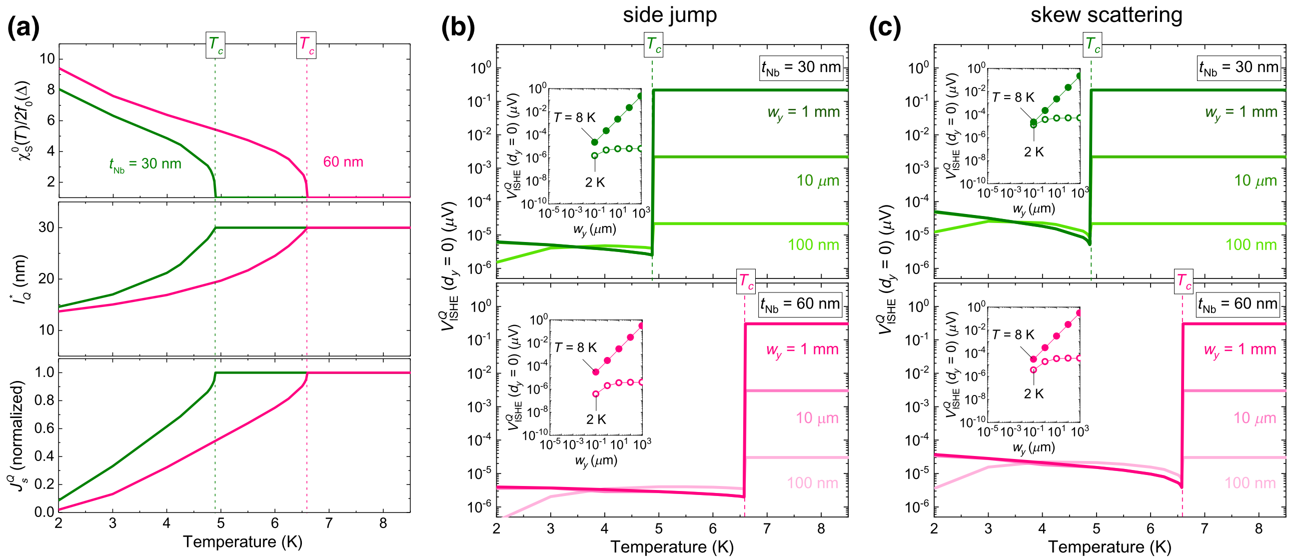

FIG. 6. (a) Calculated values of the quasiparticle (QP) spin susceptibility $\chi_S^0(T)$ divided by the QP population $2f_0(\Delta)$ (top panel), the effective spin-transport length l_Q^* (middle panel), and the spin-current density j_s^Q at a Nb/$Ni_{80}Fe_{20}$ interface (bottom panel) using Eqs. (S4)–(S6), respectively, across the superconducting transition temperature T_c of Nb. The green and pink curves represent, respectively, the superconducting Nb/$Ni_{80}Fe_{20}$ samples with the Nb thicknesses t_{Nb} of 30 and 60 nm. (b),(c) Calculated dc voltage V_{ISHE}^Q expected from the QP-mediated inverse spin-Hall effect, using Eqs. (S3)–(S6), for $t_{Nb} = 30$ (top panel) and 60 nm (bottom panel) across their T_c. Each inset presents the dependence of V_{ISHE}^Q on the active width of the precession $Ni_{80}Fe_{20}$, w_y, above and well below T_c. Figures 6(b) and 6(c) indicate, respectively, the side-jump and skew-scattering contributions. Note that a larger increase of V_{ISHE}^Q at a lower T in the skew-scattering case relative to that in the side jump reflects its strong T dependence, $\propto \chi_S^0(T)/2f_0(\Delta)$ [see Fig. 6(a), top panel] [49,50].

normalized charge susceptibility of QP [49,50]. τ_{qp} is the charge-imbalance relaxation time, τ_ϵ is the energy relaxation time, and $\Delta(T) \approx 1.76 k_B T_c \tanh[1.74\sqrt{T/T_c - 1}]$ is the superconducting energy gap. Note that $k_B T/\Delta$ represents an approximate estimate for the fraction of QPs participating in the charge imbalance [46–48]. Around T_c because τ_ε does not change significantly, $\lambda_Q(T) \propto [\Delta(T)]^{-1/2} \propto (1 - T/T_c)^{-1/4}$. By contrast below T_c, $k_B T/\Delta(T)$ is of the order of unity and this means that $\lambda_Q(T)$ is determined by $\tau_\varepsilon(T)$. If the QP charge relaxation is dominated by the inelastic electron-phonon scattering, $\tau_{in} \propto T^{-3}$ for low-energy QPs [$k_B T \ll \Delta(T)$] and thus $\lambda_Q(T) \propto T^{-3/2}$ [46–48]. Considering all of this, the overall T dependence can be approximated by $\lambda_Q(T) \approx \lambda_Q(0)[T^{-3/2} + (1 - T/T_c)^{-1/4}]$. It was previously shown from current-voltage characteristics of Nb nanobridges [51] and spin-resistance measurements in $Ni_{80}Fe_{20}$/Al_2O_3/Nb/Al_2O_3/$Ni_{80}Fe_{20}$ structures [52] that $\lambda_Q \approx 90$–150 nm and $\tau_Q \approx 13$–26 ps for Nb films immediately below T_c.

To gain further insight into the role of the factor $\lambda_Q(T)$, we calculate the transverse dc voltage V_{ISHE}^Q expected from QP-mediated ISHE in the superconducting Nb layer (Fig. 6) according to the previous theoretical work [49,50], where the QP spin Hall angle is assumed to be given by two extrinsic components of the side jump [53] and the skew scattering [54] (see Ref. [28] for details). The spin-to-charge conversion in SCs is rather complicated in that the coupling between different nonequilibrium modes (spin, charge, and energy) with Zeeman splitting [55–58] and the nonlinear kinetic equations in the superconducting states [59–61], which have not been applied yet in nonequilibrium situations, should be taken into account properly. In the calculation, we mainly consider the change of the QP charge imbalance [23,25,46,47] because of the complexity.

The most important aspect of the calculations [Figs. 6(b) and 6(c)] is that the maximum V_{ISHE}^Q at $d_y = 0$ depends insensitively on the active width of precessing FM, w_y [see Fig. 1(c)], when λ_Q becomes comparable to or shorter than w_y. Two T regimes can be identified. For $T > T_c$, V_{ISHE} scales linearly with w_y, as expected for the electromotive force in the normal state [8–10]; for $T < T_c$, V_{ISHE}^Q is almost independent of w_y. We note that in addition to the rapid decay of $\lambda_Q(T)$ across T_c, the effective spin-transport length $l_Q^*(T)$ [Fig. 6(a), middle panel] and the the QP current density $j_s^Q(T)$ [Fig. 6(a), bottom panel] are both progressively reduced as T decreases due to the

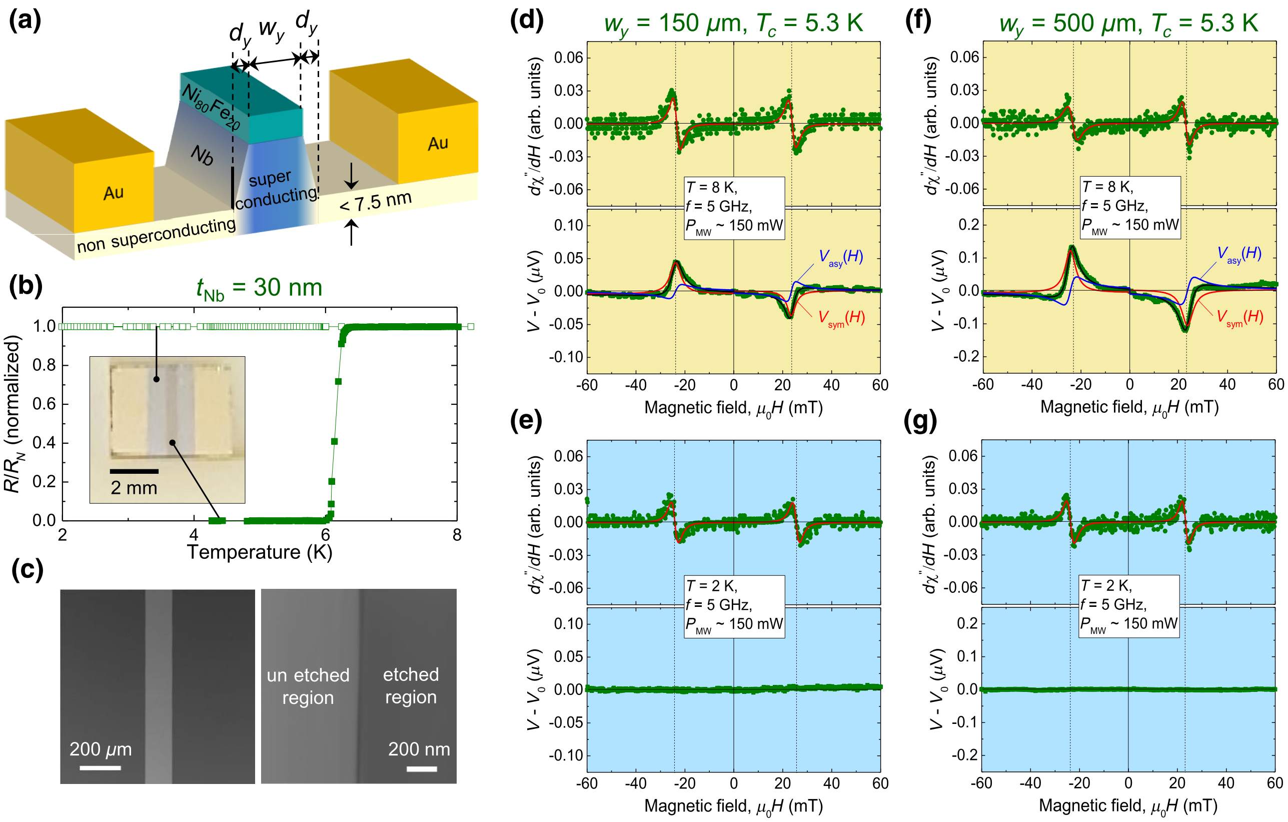

FIG. 7. (a) Schematic of the single-stripe-patterned sample, comprising an unetched $Ni_{80}Fe_{20}$/superconducting Nb bilayer at the middle and etched nonsuperconducting Nb leads (<7.5 nm) on the lateral sides of the bilayer. (b) Normalized resistance R/R_N vs temperature T plots measured at the unetched $Ni_{80}Fe_{20}$/Nb bilayer (closed green symbol) and at the etched Nb lead (open green symbol) using a four-point current-voltage method without MW excitation. (c) Scanning electron microscope images of the patterned sample. (d)–(g) Representative data of FMR absorption (top panel) and dc voltage measurements (bottom panel) for the patterned samples with the $Ni_{80}Fe_{20}$ spin-source width w_y of 150 and 500 μm, taken above and well below T_c.

development of the (singlet) superconducting gap and the freeze out of the QP population [20,25]. Thus, a vanishingly small amplitude of V^Q_{ISHE} [$\ll 1$ nV, Fig. 6(b)] is expected below T_c although a clear rise in V^Q_{ISHE} exists at a lower T, caused by the increased Nb/$Ni_{80}Fe_{20}$ bilayer resistance due to the exponential T dependence of QP resistivity [20,25].

Notwithstanding, the calculation suggests a device geometry more suited to electrical detection of the ISHE in *both* the normal and deep into the superconducting states, namely, (1) by utilizing an array of densely packed FM stripes with a periodicity that is comparable to the QP charge relaxation length of the SC and (2) by reducing the separation distance between the nearest FM stripes as much as possible. In such a proposed device, one can greatly amplify the total magnitude of spin Hall voltage by increasing the active volume of QP charge imbalance for a given reasonable P_{MW}. Importantly, from the measured value of $V_{\mathrm{sym}} = 50$–150 nV (see Fig. 6), we obtain V^Q_{ISHE} of the order of 10–100 nV, which can be *measurable* well below T_c. Detailed calculations are presented in Ref. [28].

E. Sample geometry dependence of inverse spin Hall voltages

Finally, we investigate the sample geometry dependence of ISHE voltages by using single-stripe-patterned samples to check the validity of the model calculation. These samples consist of an unetched $Ni_{80}Fe_{20}$ or superconducting Nb bilayer at the middle and etched nonsuperconducting Nb leads (<7.5 nm) on the lateral sides of the bilayer [Figs. 7(a) and 7(b)]. We note that in such patterned samples, d_y can effectively be reduced to a few tens of nm, as probed by a scanning electron microscope [Fig. 7(c)]. Figures 7(d)–7(g) exhibit the representative data of FMR absorption (top panel) and dc voltage measurements (bottom panel) vs $\mu_0 H$ along the x axis for two different w_y of 150 and 500 μm, taken above and well below T_c. In the normal state ($T > T_c$), V_{sym} of $w_y = 500$ μm is approximately three times greater than of $w_y = 150$ μm, in accordance with the model calculation, whereas in the superconducting state ($T < T_c$), no voltage signal is observed for both cases. It is notable that the sign of V_{sym} above T_c is reversed from the preceding experiment with Nb/$Ni_{80}Fe_{20}$ structure (see Fig. 2) because the direction of J_S is reversed in the $Ni_{80}Fe_{20}$/Nb inverted structure, providing an additional evidence of the spin Hall voltages from the Nb [8–10].

The vanishing of the ISHE voltage for the patterned samples ($d_y \leq 30$ nm) well below T_c suggests the rapid decay of λ_Q of Nb as T_c is crossed. These results are in contrast to a previous observation of the giant ISHE induced by electrical spin injection from $Ni_{80}Fe_{20}$ through Cu into superconducting NbN ($d_y \approx 400$ nm) far below T_c [25]. However, a recent report on the ISHE voltage produced by the spin Seebeck effect in a YIG/NbN bilayer measurable only in a limited T range right below T_c [26] is more consistent with our findings. We note further that λ_Q is typically larger than the superconducting coherence length ξ_{SC} and comparable to l_{sd} at a lower T in the experiments performed to date [46–48]; thus it appears that a shorter λ_Q is predicted in NbN relative to Nb [20,25]. The exact origin of the observed differences between experiments is not yet clear although different materials, device geometry, contact property, spin-injection method, and spin-orbit coupling mechanism will undoubtably have an influence, requiring further investigation. A natural starting point for further work is to develop a spin Hall device [62] that works reliably in both the normal and (deep into) the superconducting states with a reasonable driving power density, as proposed here.

IV. CONCLUSIONS

We experimentally estimate the RT values of θ_{SH}, l_{sd}, and τ_{sf} of Nb films from spin-pumping-induced ISHE measurements in Nb/$Ni_{80}Fe_{20}$ bilayers by varying t_{Nb}, comparing to a $Ni_{80}Fe_{20}$/Pt reference sample, and measuring an out-of-plane angular dependence. We also study the ISHE as a function of T for different t_{Nb}. Above T_c of Nb, a clear t_{Nb}-dependent T evolution of the ISHE is observed whereas below T_c, the ISHE voltage drops abruptly and becomes undetectable at a lower T. This can be understood in terms of the strong decay of λ_Q across T_c of the Nb, as supported by the additional investigation of the ISHE in a different sample geometry along with model calculation. Our results suggest that the QP charge-imbalance relaxation length (of superconducting Nb) is shorter than hitherto assumed and needs to be considered in the development of new spin-pumping and spin-torque FMR devices [62] that aim to utilize QP spin-to-charge conversion and vice versa, respectively.

ACKNOWLEDGMENTS

This work is supported by EPSRC Programme Grant EP/N017242/1.

[1] S. O. Valenzuela and M. Trinkham, Direct electronic measurement of the spin Hall effect, Nature **442**, 176 (2006).

[2] T. Kimura, Y. Otani, and J. Hamrle, Switching Magnetization of a Nanoscale Ferromagnetic Particle Using Nonlocal Spin Injection, Phys. Rev. Lett. **96**, 037201 (2006).

[3] L. Berger, Emission of spin waves by a magnetic multilayer traversed by a current, Phys. Rev. B **54**, 9353 (1996).

[4] J. A. Katine, F. J. Albert, R. A. Buhrman, E. B. Myers, and D. C. Ralph, Current-Driven Magnetization Reversal and Spin-Wave Excitations in Co/Cu/Co Pillars, Phys. Rev. Lett. **84**, 3149 (2000).

[5] V. E. Demidov, S. Urazhdin, E. Edwards, M. Stiles, R. McMichael, and S. Demokritov, Control of Magnetic Fluctuations by Spin Current, Phys. Rev. Lett. **107**, 107204 (2011).

[6] S. Mizukami, Y. Ando, and T, Miyazaki, Effect of spin diffusion on Gilbert damping for a very thin permalloy layer in Cu/permalloy/Cu/Pt films, Phys. Rev. B **66**, 104413 (2002).

[7] Y. Tserkovnyak, A. Brataas, G. E. W. Bauer, and B. I. Halperin, Nonlocal magnetization dynamics in ferromagnetic heterostructures, Rev. Mod. Phys. **77**, 1375 (2005).

[8] E. Saitoh, M. Ueda, H. Miyajima, and G. Tatara, Conversion of spin current into charge current at room temperature: Inverse spin-Hall effect, Appl. Phys. Lett. **88**, 182509 (2006).

[9] K. Ando, S. Takahashi, J. Ieda, Y. Kajiwara, H. Nakayama, T. Yoshino, K. Harii, Y. Fujikawa, M. Matsuo, S. Maekawa, and E. Saitoh, Inverse spin-Hall effect induced by spin pumping in metallic system, J. Appl. Phys. **109**, 103913 (2011).

[10] G. E. W. Bauer, E. Saitoh, and B. J. van Wees, Spin caloritronics, Nat. Mater. **11**, 391 (2012).

[11] K. Ando, S. Takahashi, J. Ieda, H. Kurebayashi, T. Trypiniotis, C. H. W. Barnes, S. Maekawa, and E. Saitoh, Electrically tunable spin injector free from the impedance mismatch problem, Nat. Mater. **10**, 655 (2011).

[12] K. Ando, S. Watanabe, S. Mooser, E. Saitoh, and H. Sirringhaus, Solution-processed organic spin–charge converter, Nat. Mater. **12**, 622 (2013).

[13] E. Lesne, Y. Fu, S. Oyarzun, J. C. Rojas-Sanchez, D. C. Vaz, H. Naganuma, G. Sicoli, J. P. Attane, M. Jamet, E. Jacquet, J. M. George, A. Barthelemy, H. Jaffres, A. Fert, M. Bibes, and L. Vila, Highly efficient and tunable spin-to-charge conversion through Rashba coupling at oxide interfaces, Nat. Mater. **15**, 1261 (2016).

[14] R. Ohshima, Y. Ando, K. Matsuzaki, T. Susaki, M. Weiler, S. Klingler, H. Huebl, E. Shikoh, T. Shinjo, S. T. B. Goennenwein, M. Shiraishi, Strong evidence for d-electron spin transport at room temperature at a $LaAlO_3/SrTiO_3$ interface, Nat. Mater. **16**, 609 (2017).

[15] Y. Shiomi, K. Nomura, Y. Kajiwara, K. Eto, M. Novak, K. Segawa, Y. Ando, and E. Saitoh, Spin-Electricity Conversion Induced by Spin Injection into Topological Insulators, Phys. Rev. Lett. **113**, 196601 (2014).

[16] J.-C. Rojas-Sánchez, S. Oyarzún, Y. Fu, A. Marty, C. Vergnaud, S. Gambarelli, L. Vila, M. Jamet, Y. Ohtsubo, A. Taleb-Ibrahimi, P. Le Fèvre, F. Bertran, N. Reyren, J.-M. George, and A. Fert, Spin to Charge Conversion at Room Temperature by Spin Pumping into a New Type of Topological Insulator: α-Sn Films, Phys. Rev. Lett. **116**, 096602 (2016).

[17] J. Linder, and J. A. W. Robinson, Superconducting spintronics, Nat. Phys. **11**, 307 (2015).

[18] D. Beckmann, Spin manipulation in nanoscale superconductors, J. Phys.: Condens. Matter **28**, 163001 (2016).

[19] F. Hübler, M. J. Wolf, D. Beckmann, D. and H. v. Löhneysen, Long-Range Spin-Polarized Quasiparticle Transport in Mesoscopic Al Superconductors with a Zeeman Splitting, Phys. Rev. Lett. **109**, 207001 (2012).

[20] J. Y. Gu, J. A. Caballero, R. D. Slater, R. Loloee, and W. P. Pratt, Direct measurement of quasiparticle evanescent waves in a dirty superconductor, Phys. Rev. B **66**, 140507(R) (2002).

[21] H. Yang, S-H. Yang, S. Takahashi, S. Maekawa, and S. S. P. Parkin, Extremely long quasiparticle spin lifetimes in superconducting aluminium using MgO tunnel spin injectors, Nat. Mater. **9**, 586 (2010).

[22] N. Poli, J. P. Morten, M. Urech, Arne Brataas, D. B. Haviland, and V. Korenivski, Spin Injection and Relaxation in a Mesoscopic Superconductor, Phys. Rev. Lett. **100**, 136601 (2008).

[23] C. H. L. Quay, D. Chevallier, C. Bena, and M. Aprili, Spin imbalance and spin-charge separation in a mesoscopic superconductor, Nat. Phys. **9**, 84 (2013).

[24] T. Wakamura, N. Hasegawa, K. Ohnishi, Y. Niimi, and Y. Otani, Spin Injection into a Superconductor with Strong Spin-Orbit Coupling, Phys. Rev. Lett. **112**, 036602 (2014).

[25] T. Wakamura, H. Akaike, Y. Omori, Y. Niimi, S. Takahashi, A. Fujimaki, S. Maekawa, and Y. Otani, Quasiparticle-mediated spin Hall effect in a superconductor, Nat. Mater. **14**, 675 (2015).

[26] M. Umeda, Y. Shiomi, T. Kikkawa, T. Niizeki, J. Lustikova, S. Takahashi, and E. Saitoh, Spin-current coherence peak in superconductor/magnet junctions, arXiv:1801.07943.

[27] K.-R. Jeon, C. Ciccarelli, A. J. Ferguson, H. Kurebayashi, L. F. Cohen, X. Montiel, M. Eschrig, J. W. A. Robinson, and M. G. Blamire, Enhanced spin pumping into superconductors provides evidence for superconducting pure spin currents, Nat. Mater. **17**, 499 (2018).

[28] See Supplemental Material at http://link.aps.org/supplemental/10.1103/PhysRevApplied.10.014029 for a detailed analysis of the effect of MW power on the superconductivity of Nb, MW frequency dependence of FMR spectra, proposal of the device geometry for amplifying QP spin-Hall voltages, control experiment on a Nb/$Ni_{80}Fe_{20}$/Nb symmetric structure, inverse spin-Hall voltages in the vicinity of T_c, and theoretical description of QP-mediated spin-Hall voltages.

[29] L. Chen, F. Matsukura, and H. Ohno, Direct-current voltages in (Ga,Mn)As structures induced by ferromagnetic resonance, Nat. Commun. **4**, 2055 (2013).

[30] A. Azevedo, L. Vilela-Leão, R. Rodríguez-Suárez, A. L. Santos, and S. Rezende, Spin pumping and anisotropic magnetoresistance voltages in magnetic bilayers: Theory and experiment, Phys. Rev. B **83**, 144402 (2011).

[31] R. Iguchi and E. Saitoh, Measurement of spin pumping voltage separated from extrinsic microwave effects, J. Phys. Soc. Jpn. **86**, 011003 (2017).

[32] J.-C. Rojas-Sánchez, N. Reyren, P. Laczkowski, W. Savero, J.-P. Attané, C. Deranlot, M. Jamet, J.-M. George, L. Vila, and H. Jaffrès, Spin Pumping and Inverse Spin Hall Effect in Platinum: The Essential Role of Spin-Memory Loss at Metallic Interfaces, Phys. Rev. Lett. **112**, 106602 (2014).

[33] M. Morota, Y. Niimi, K. Ohnishi, D. H. Wei, T. Tanaka, H. Kontani, T. Kimura, and Y. Otani, Indication of intrinsic spin Hall effect in 4d and 5d transition metals, Phys. Rev. B **83**, 174405 (2011).

[34] J. M. Shaw, H. T. Nembach, T. J. Silva, and C. T. Boone, Precise determination of the spectroscopic g-factor by use of broadband ferromagnetic resonance spectroscopy, J. Appl. Phys. **114**, 243906 (2013).

[35] S. Gupta, R. Medwal, D. Kodama, K. Kondou, Y. Otani, and Y. Fukuma, Important role of magnetization precession angle measurement in inverse spin Hall effect induced by spin pumping, Appl. Phys. Lett. **110**, 022404 (2017).

[36] T. Tanaka, H. Kontani, M. Naito, T. Naito, D. S. Hirashima, K. Yamada, and J. Inoue, Intrinsic spin Hall effect and orbital Hall effect in 4d and 5d transition metals, Phys. Rev. B **77**, 165117 (2008).

[37] K.-R. Jeon, B.-C. Min, Y.-H. Park, S.-Y. Park, and S.-C. Shin, Electrical investigation of the oblique Hanle effect in ferromagnet/oxide/semiconductor contacts, Phys. Rev. B **87**, 195311 (2013).

[38] W. Hanle, Über magnetische Beeinflussung der Polarisation der Resonanzfluoreszenz, Z. Phys. **30**, 93 (1924).

[39] V. F. Motsnyi, P. Van Dorpe, W. Van Roy, E. Goovaerts, V. I. Safarov, G. Borghs, and J. De Boeck, Optical investigation of electrical spin injection into semiconductors, Phys. Rev. B **68**, 245319 (2003).

[40] K. Ando and E. Saitoh, Observation of the inverse spin Hall effect in silicon, Nat. Commun. **3**, 629 (2012).

[41] A. Tsukahara, Y. Ando, Y. Kitamura, H. Emoto, E. Shikoh, M. P. Delmo, T. Shinjo, and M. Shiraishi, Self-induced inverse spin Hall effect in permalloy at room temperature, Phys. Rev. B **89**, 235317 (2014).

[42] E. Sagasta, Y. Omori, M. Isasa, Y. Otani, L. E. Hueso, and F. Casanova, Spin diffusion length of Permalloy using spin absorption in lateral spin valves, Appl. Phys. Lett. **111**, 082407 (2017).

[43] J. P. Morten, A. Brataas, G. E. W. Bauer, W. Belzig, and Y. Tserkovnyak, Proximity-effect–assisted decay of spin currents in superconductors, Eur. Phys. Lett. **84**, 57008 (2008).

[44] M. Inoue, M. Ichioka, and H. Adachi, Spin pumping into superconductors: A new probe of spin dynamics in a superconducting thin film, Phys. Rev. B **96**, 024414 (2017).

[45] C. Bell, S. Milikisyants, M. Huber, and J. Aarts, Spin Dynamics in a Superconductor-Ferromagnet Proximity System, Phys. Rev. Lett. **100**, 047002 (2008).

[46] P. Cadden-Zimansky, Z. Jiang, and V. Chandrasekhar, Charge imbalance, crossed Andreev reflection and elastic co-tunnelling in ferromagnet/superconductor/normal-metal structures, New J. Phys. **9**, 116 (2007).
[47] F. Hübler, J. Camirand Lemyre, D. Beckmann, and H. v. Löhneysen, Charge imbalance in superconductors in the low-temperature limit, Phys. Rev. B **81**, 184524 (2010).
[48] T. E. Golikova, M. J. Wolf, D. Beckmann, I. E. Batov, I. V. Bobkova, A. M. Bobkov, and V. V. Ryazanov, Nonlocal supercurrent in mesoscopic multiterminal SNS Josephson junction in the low-temperature limit, Phys. Rev. B **89**, 104507 (2014).
[49] S. Takahashi and S. Maekawa, Hall Effect Induced by a Spin-Polarized Current in Superconductors, Phys. Rev. Lett. **88**, 116601 (2002).
[50] S. Takahashi and S. Maekawa, Spin Hall effect in superconductors, Jpn. J. Appl. Phys. **51**, 010110 (2012).
[51] K. N. Tu and R. Rosenberg, eds. *Preparation and Properties of Thin Films* (Elsevier, Amsterdam, 1984).
[52] M. Johnson, Spin coupled resistance observed in ferromagnet-superconductor-ferromagnet trilayers, Appl. Phys. Lett. **65**, 1460 (1994).
[53] J. Smit, The spontaneous Hall effect in ferromagnetics, Physica **21**, 877 (1955); J. Smit, The spontaneous hall effect in ferromagnetics, Physica, **24**, 39 (1958).
[54] L. Berger, Side-jump mechanism for the Hall effect of ferromagnets, Phys. Rev. B **2**, 4559 (1970).
[55] F. Sebastian Bergeret, Mikhail Silaev, Pauli Virtanen, and Tero T. Heikkila, Nonequilibrium effects in superconductors with a spin-splitting field, arXiv:1706.08245.
[56] M. Trif and Y. Tserkovnyak, Dynamic Magnetoelectric Effect in Ferromagnet/Superconductor Tunnel Junctions, Phys. Rev. Lett. **111**, 087602 (2013).
[57] M. Silaev, P. Virtanen, F. S. Bergeret, and T. T. Heikkilä, Long-Range Spin Accumulation from Heat Injection in Mesoscopic Superconductors with Zeeman Splitting, Phys. Rev. Lett. **114**, 167002 (2015).
[58] I. V. Bobkova and A. M. Bobkov, Injection of nonequilibrium quasiparticles into Zeeman-split superconductors: A way to create long-range spin imbalance, Phys. Rev. B **93**, 024513 (2016).
[59] F. Konschelle, Ilya V. Tokatly, and F. Sebastián Bergeret, Theory of the spin-galvanic effect and the anomalous phase shift φ_0 in superconductors and Josephson junctions with intrinsic spin-orbit coupling, Phys. Rev. B **92**, 125443 (2015).
[60] F. Sebastian Bergeret and Ilya V. Tokatly, Manifestation of extrinsic spin Hall effect in superconducting structures: Nondissipative magnetoelectric effects, Phys. Rev. B **94**, 180502(R) (2016).
[61] I. V. Tokatly, Usadel equation in the presence of intrinsic spin-orbit coupling: A unified theory of magnetoelectric effects in normal and superconducting systems, Phys. Rev. B **96**, 060502(R) (2017).
[62] Y. Otani, M. Shiraishi, A. Oiwa, E. Saitoh, and S. Murakami, Spin conversion on the nanoscale, Nat. Phys. **3**, 829 (2017).